Thin Cloud Removal Based on Signal Transmission Principles and Spectral Mixture Analysis

Meng Xu, *Student Member, IEEE*, Mark Pickering, *Member, IEEE*,
Antonio J. Plaza, *Fellow, IEEE*, and Xiuping Jia, *Senior Member, IEEE*

Abstract—Cloud removal is an important goal for enhancing the utilization of optical remote sensing satellite images. Clouds dynamically affect the signal transmission due to their different shapes, heights, and distribution. In the case of thick opaque clouds, pixel replacement has been commonly adopted. For thin clouds, pixel correction techniques allow the effects of thin clouds to be removed while retaining the remaining information in the contaminated pixels. In this paper, we develop a new method based on signal transmission and spectral mixture analysis for pixel correction which makes use of a cloud removal model that considers not only the additive reflectance from the clouds but also the energy absorption when solar radiation passes through them. Data correction is achieved by subtracting the product of the cloud endmember signature and the cloud abundance and rescaling according to the cloud thickness. The proposed method has no requirement for meteorological data and does not rely on reference images. Our experimental results indicate that the proposed approach is able to perform effective removal of thin clouds in different scenarios.

Index Terms—Cloud removal, cloud thickness, data correction, signal transmission, spectral unmixing.

I. Introduction

REMOTE sensing satellite images generated using frequencies in the optical to microwave electromagnetic spectrum have been widely applied in Earth Observation. Optical remote sensing, in particular, is popular since it is relatively easier to interpret and analyze. Recently, new optical multispectral data have become available from Landsat 8 Operational Land Imager (OLI), which was launched in 2013 [1] and SPOT 7, which was launched in June 2014 (http://www.astrium-geo.com) These sensors provide continued monitoring of land surface, ocean, and atmosphere with medium and high spatial resolution. However, one of the primary limitations of optical sensors is their sensitivity to atmospheric conditions. Cloud cover is a key problem which degrades the utilization of optical data and increases the difficulty of image analysis [2], [3]. Clouds dynamically affect the electromagnetic signal transmission due

to their different shapes, heights, and distribution. Thick opaque clouds may block all the reflectance from the Earth's surface, while thin transparent clouds attenuate the incident energy to the ground and contaminate the upwelling signal received by the sensor [4]. Data replacement for the blocked areas and data correction for the distorted pixels are a valuable pre-processing step to restore the quality of collected images for subsequent applications. [5] proposed a method which uses similar pixels in neighboring areas of the target image to fill the blocked pixels, and multitemporal data are required as a reference to identify similar pixels. In addition, Li *et al.* [6] introduced a multitemporal dictionary learning approach to achieve thick cloud replacement. In this paper, we mainly address the data correction issue, i.e., removing the effect caused by thin clouds.

To derive cloud free images, identifying cloud affected pixels using cloud detection techniques is a primary task. An automated cloud-cover assessment (ACCA) algorithm was designed to estimate the fraction of cloud cover in images captured by the ETM+ on Landsat 7. ACCA makes use of the spectral properties of landscape features and cloud signatures in the thermal band (Band 6 of ETM+) to mask cloudy pixels [7], [8]. In [9], the author developed the function of mask (Fmask) algorithm for detecting cloud and cloud shadow in Landsat imagery over land and water, separately. Fmask improved the cloud detection performance when compared with ACCA and addressed the snow interference issue. Several methods, using multispectral analysis, have been proposed to identify cloud cover based on an assumption that cloud is normally brighter and colder than the underlying land surface [10], [11]; however these methods will fail when the cloud is relatively thin and warm [9]. Gao *et al.* [12] proposed a method to detect cirrus cloud using the 1.38 μm band from MODIS. This short wave infrared band has very strong water vapor absorption, such that only high level clouds in the atmosphere are visible in this narrow band and the ground appears totally black [13]. A multi-temporal cloud detection (MTCD) method was presented in [14] by taking advantage of the high revisit frequency of Landsat sensors and was shown to be able to identify any significant increases in reflectance on a per pixel basis between cloudy images and cloud-free images acquired on different dates. However, the result produced by MTCD is strongly dependent on the quality of the reference images. More sophisticated detection methods have been proposed in recent years based on image fusion [15], [16], neural networks [17] and a Bayesian approach [18].

Several methods have been developed to retrieve the reflectance from the objects beneath the cloud. The dark object subtraction algorithm [19], [20] is simple and effective for approximate bulk correction of atmospheric effects, with no

requirement for meteorological data [4]. The haze optimized transformation (HOT) was proposed in [21] based on the observation that spectral responses of various types of land surfaces in the red band have high correlation to the blue band under clear atmospheric conditions [22]. This linear relationship will be contaminated when clouds are present. Therefore, cloud removal was implemented by moving the cloudy pixels' data to the clear line which represents the linear relationship of the two bands in spectral space. A principal component based haze masking approach was developed in [23] which combines spatial and spectral features of cloud in the transformed space. While these image-based methods are easy to implement, the signal transmission theory is not considered.

A physical cloud distortion model was first developed in [24] to describe the sunlight transmission process in the presence of clouds. This model treats clouds as low frequency noise effects and makes use of a Wiener filter to separate the signal from the noise. Kechu and Wentao [25] improved this model by establishing a mathematical model for various layers of clouds. To apply this model, there is a need to know the noise statistics of the clouds, which has to be estimated since it is not available *a priori* [26]. Shen *et al.* [27] developed a locally adaptive thin cloud removal algorithm which was executed in the frequency domain. In [28], the authors used a Kaiser window function to estimate noise statistics in cloudy images. A problem encountered in this approach is that it is difficult to identify the densities of the cloud cover in optical images [29]. Another weakness of these models is the lack of consideration of cloud absorption. In this paper, we develop an improved cloud model to include the cloud absorptance in the signal transmission path.

Alternatively several cloud screening methods have been developed based on spectral unmixing techniques [30]–[32]. Due to limited spatial resolution, most pixels in a remote sensing image are mixed pixels and they contain more than one ground cover type (endmember classes). The spectrum of a pixel recorded by satellite scanners is often a mixture of the reflectance from more than one distinct material. Spectral unmixing techniques have been developed to find the fraction (abundance) of each endmember class [33]–[35]. The paper [30] treated cloud as one of the endmember classes and selected a pure cloud spectrum as the endmember to represent the cloud signature. The cloud-abundance product is obtained after mixture model inversion. A linear mixture of cloud and background modeled for MODIS radiance was proposed in [32], where cloud fractions were estimated by a multiple-kernel learning-based unmixing algorithm. These methods yield subpixel cloud fraction results. Cloud effect removal, however, was not addressed. In this paper, we combine spectral unmixing analysis with the physical model to achieve data correction.

More specifically, we develop a new cloud removal method based on signal transmission and spectral mixture analysis (ST-SMA) which considers not only the additive reflectance from clouds but also the energy absorption when solar radiation passes through them. Spectral unmixing is applied to estimate cloud thickness, which is equivalent to the cloud abundance fraction within a pixel. Data correction is finally achieved by subtracting the product of the cloud endmember signature and the cloud abundance and rescaling according to the cloud thickness.

The rest of this paper is organized as follows. Section II briefly reviews related work on physical cloud distortion modeling and linear spectral mixture analysis used in cloud mapping. Section III describes the proposed method ST-SMA for modeling cloud effects and correcting cloud contamination. Section IV presents a series of experiments to validate the ST-SMA approach. Finally, discussions and conclusions are given in Section V.

II. RELATED WORK

A. Cloud Distortion Model

A physical model of cloud distortion was first developed in [24]. The authors assumed that the received signal at the sensor is given by

$$s(x,y) = aIr(x,y)t(x,y) + I[1 - t(x,y)] \quad (1)$$

where I is the solar irradiance, $r(x,y)$ is the reflectance from ground, and $t(x,y)$ is the cloud transmittance. a is the sunlight attenuation coefficient. The values of a, $r(x,y)$ and $t(x,y)$ range from 0 to 1. The first part of (1) indicates the degraded reflectance from the ground, and the second part denotes the reflected signal from cloud with an assumption of 0% cloud absorption. After subtracting $s(x,y)$ from I and taking the logarithm, we obtain

$$\log[I - s(x,y)] = \log[I - aIr(x,y)] + \log[t(x,y)] \quad (2)$$

where $\log[I - aIr(x,y)]$ and $\log[t(x,y)]$ are associated with the original signal and cloud noise, respectively. Thus, cloud removal can be conducted by using a homomorphic Weiner filter in the frequency domain by assuming that clouds contain only low spatial frequencies.

This distortion model considers the spectral characteristics of clouds. It treats the sum of reflectance and transmittance from cloud as one, with an assumption of zero cloud absorption. Therefore, the loss of radiation energy when passing through clouds is not considered. In fact, clouds have variable structure and thickness. Therefore, it is important to quantify the loss of energy when estimating cloud effects. Another weakness of this method is that there is a need to estimate the noise statistics of the cloud, which is nontrivial.

B. Cloud Assessment Using Spectral Unmixing Techniques

The limited spatial resolution of sensors and the complexity of Earth surface materials usually lead to mixed pixels in most areas of a remote sensing image. Spectral unmixing is a technique that is used to address the mixture problem by decomposing a mixed spectrum into a fractional set of spectra of pure materials (known as endmembers) [33], [35]. Cloud assessment using spectral unmixing techniques has taken the approach of treating cloud as one of the endmembers. Suppose there are M endmembers in the mixed pixel. When a linear mixture model is applied, the reflected solar electromagnetic radiation $\mathbf{x}$ can be expressed as

$$\mathbf{x} = \sum_{m=1}^{M} a_m \mathbf{s}_m + \mathbf{e} = \mathbf{Sa} + \mathbf{e} \quad (3)$$

where $\mathbf{x}$ is an $L \times 1$ column vector, representing the reflectance of the observed pixel, L is the number of spectral bands in the image, $\mathbf{S} = (\mathbf{s_1}, \ldots, \mathbf{s_M})$ denotes an $L \times M$ endmember signature matrix whose mth column vector represents the mth endmember signature. $\mathbf{a} = (a_1, \ldots, a_M)^T$ is an $M \times 1$ abundance vector representing the fraction of each endmember. $\mathbf{e}$ is an $L \times 1$ noise vector which can be considered as model error.

A cloud-screening algorithm that used spectral unmixing techniques to produce a cloud abundance map instead of binary indicators for cloud or non-cloud was developed in [30]. In their model, cloud is assumed to be one of the endmember classes, and its mean spectrum was chosen as the endmember to represent the cloud signature. Cloud fractions can be obtained by inverting (3)

$$\mathbf{a} = (\mathbf{S^T S})^{-1} \mathbf{S^T x}. \tag{4}$$

The linear spectral mixture model (LSMM) is usually subject to the following two constraints to make the results meaningful:

1) Sum-to-one:

$$\sum_{m=1}^{M} a_m = 1. \tag{5}$$

2) Nonnegativity:

$$a_m \geq 0. \tag{6}$$

This approach is referred to as fully constrained linear mixture analysis [36].

In this method, the reflectances from the ground cover types and from cloud are considered separately. The attenuation of the sunlight during the propagation of cloud is ignored. It is also worth noting that this method is mainly for cloud assessment. While the cloud fractions were mapped, cloud effect removal could bring additional issues, which were not presented in [30].

In this paper, we address the aforementioned issues by presenting a new method, ST-SMA, which can estimate the absorption and transmission for various thicknesses of cloud, and achieve cloud removal with the aid of spectral unmixing techniques.

III. PROPOSED METHOD

A. Physical Cloud Effect Modeling

The proposed cloud removal method ST-SMA starts with the application of an electromagnetic energy balance equation. During propagation of solar radiation, scattering and absorption occurs [37]. Scattering can occur in two ways, reflection and transmission. The sum of reflected, transmitted, and absorbed radiation equals the incident radiation according to the law of conservation of energy [38]. This fact can be expressed as

$$I = R + A + T \tag{7}$$

where I is the incident radiation, R is the reflected radiation, A is the absorbed radiation, and T is the transmitted radiation. If we use reflectance ρ_r, absorptance ρ_a, and transmittance ρ_t to
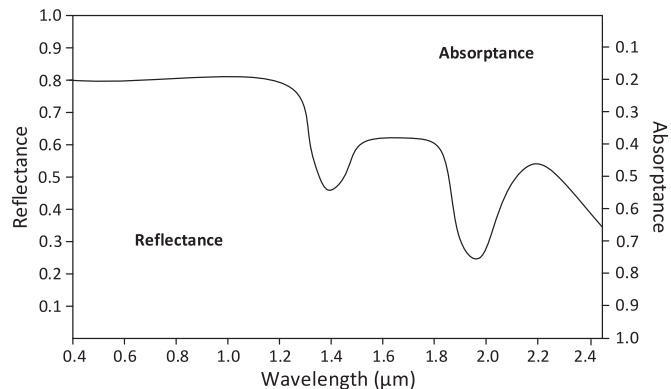

Fig. 1. Spectral reflectance and absorptance of an opaque cloud.

describe (7), then $R = \rho_r I$, $A = \rho_a I$ and $T = \rho_t I$. (7) can be rewritten as

$$\rho_r + \rho_a + \rho_t = 1. \tag{8}$$

Based on this principle, we propose a means to estimate cloud transmittance as a function of cloud thickness. We first consider the relationship between an opaque cloud's spectral reflectance and its absorptance, as shown in Fig. 1. We regard this case as zero transmittance, i.e., no sunlight is transmitted through the opaque cloud and all the remaining energy is absorbed by cloud after reflection. Therefore, the absorptance of opaque clouds is given by

$$\rho_a = 1 - \rho_r, \tag{9}$$

where ρ_r and ρ_a are the reflectance and absorptance of opaque cloudy pixels in the given band l, respectively. In this case, transmittance $\rho_t = 0$.

To find the cloud absorptance, the cloud spectral reflectance characteristics need to be defined. While there is a general understanding of high reflectance over the wide range of spectral wavelengths from visible to mid infrared, the cloud spectrum is more reliably extracted from the image data of the current scene to accommodate the local conditions. We assume that pure cloud pixels exist in the cloudy imagery, and this pure cloud is opaque enough to block all sunlight from reaching the Earth's surface. In general, thick clouds are much brighter than the land surface in visible bands. It should be mentioned that snow also emerges with very high reflectance in visible bands. Therefore, the presence of snow may cause errors in the cloud spectrum extraction process. However, snow reflectance drops significantly in shortwave-infrared bands while cloud still reflects a large proportion of solar radiation in this spectral region [39]. According to these characteristics of clouds, we propose to extract the cloud signature by searching for

$$\arg \max_n \sum_{l=1}^{L} x_n(l), \ n = 1, 2, \ldots, N \tag{10}$$

where $x_n(l)$ is the reflectance of the nth pixel in the lth spectral band. L and N are the number of bands and total number of pixels in the image, respectively. If the sum of reflectances at each band x_n is maximal, then the pixel is regarded as pure cloud. To reduce the effect of noise, the top few pixels may be identified, and their averaged spectrum is adopted as the cloud
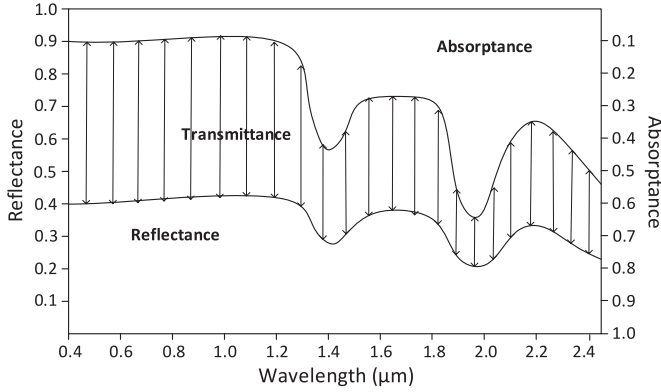
Fig. 2. Spectral response of transparent thin cloud (reflection, absorption, and transmission).

Fig. 3. Diagram of the cloud effect model.

spectrum. Let $\mathbf{s_c}$ be the vector representing the cloud spectrum, which will be used in the following derivation.

Obviously thinner clouds reflect less and absorb less, and hence transmittance is no longer zero. Let Γ represent cloud thickness. When $\Gamma = 1$, we have the case of opaque cloud. If $\Gamma = 0$, we have the cloud free case, which means 100% transmittance without reflection and absorption. Γ lies between 0 and 1 in other cases. Fig. 2 depicts the relationship between reflection, absorption, and transmission when solar radiation propagates through transparent thin clouds. We assume the reduced reflectance and absorptance, which become $\Gamma\rho_r$ and $\Gamma\rho_a$ at a given band l, respectively, are both proportional to the thickness factor Γ. For example, if $\Gamma = 0.2$, the reflectance and the absorptance will be reduced by 20%, then the transmittance through the cloud is $1 - 0.2\rho_r - 0.2\rho_a = 0.8$ (note that $\rho_r + \rho_a = 1$ for opaque clouds). Based on (8) and (9) the thin cloud transmittance $\hat{\rho}_t$ can be defined by

$$\hat{\rho}_t = 1 - \Gamma\rho_r - \Gamma\rho_a = 1 - \Gamma. \tag{11}$$

This represents the transmitted radiation that reaches the Earth's surface. Fig. 3 illustrates the signal interactions between the sun, the cloud, and the Earth's surface. If the spectral reflectance of a given pixel on the ground is $\mathbf{r}$ (an $L \times 1$ vector), the signal collected at the sensor becomes

$$\mathbf{x} = (1 - \Gamma)\mathbf{r} + \Gamma\mathbf{s_c} + \mathbf{e} \tag{12}$$

where $\mathbf{x}$ is an $L \times 1$ column vector representing the observed pixel value and $\Gamma\mathbf{s_c}$ denotes the contributed reflectance from cloud. (12) represents the physical model of the effect of cloud on the recorded signals. In (12), there are $L + 1$ unknowns in the L simultaneous equations, apart from the error term. They are the cloud thickness Γ and the reflectance at L bands, $\mathbf{r}$, of the given pixel. Therefore, cloud removal cannot be resolved using this model alone. In the next section, we introduce spectral mixture analysis to solve this problem.

B. Geometric Modeling of Mixed Pixels on the Ground

Considering the pixel on the ground which receives the attenuated solar radiation due to the cloud effect, the reflected signal is determined by the spectral characteristics of the materials present in the corresponding pixel. Often there is more than
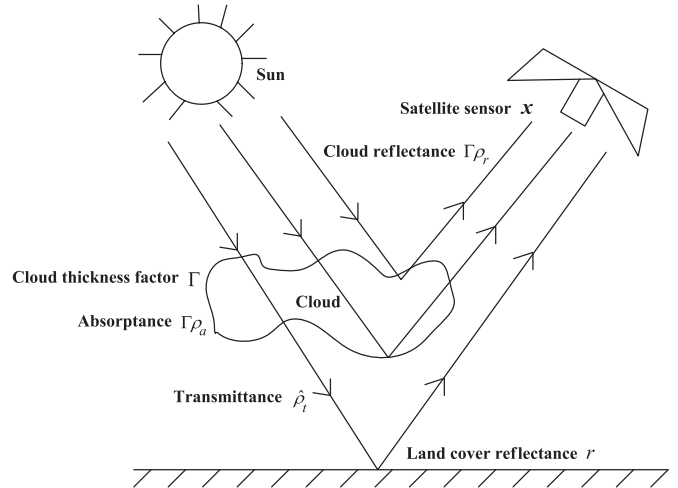
one material due to the limited spatial resolution of the sensors. We adopt linear spectral unmixing techniques to decompose the reflected signal from the ground, $\mathbf{r}$, as a weighted sum of M endmembers as follows:

$$\mathbf{r} = \sum_{m=1}^{M} a_m \mathbf{s}_m + \mathbf{e} \tag{13}$$

where a_m is the proportion of the mth endmember. To make the analysis meaningful, fully constrained least squares unmixing can be applied [36]. a_m can be interpreted as the fraction of a pixels area that the mth endmember occupies. Therefore, we can call this model a geometric description. (13) is different from (3). In (3), cloud is one of the endmember classes, which is not the case in (13). In our cloud model, we separate cloud from the other materials present in the pixel on the Earth's surface.

Endmember extraction is an important issue to address. A large number of unsupervised endmember extraction algorithms (EEAs) have been developed, e.g., Pixel Purity Index [40], [41], N-FINDR [42], vertex component analysis (VCA) [43], and minimum volume constrained non-negative matrix factorization [44], among many others [35]. When these methods are applied, a cloud endmember may be identified as well. However, in our method the cloud endmember needs to be treated separately as discussed in the next section. Supervised endmember extraction is more effective, when training data for pure classes are available to use. The endmember spectrum can be derived by averaging the training data. When the number of endmembers is fewer than the number of measurements, i.e., the number of spectral bands, an overdetermined problem is formed which can reduce the effect of noise and provide better estimates of the fraction of each endmember class using the least squares solution.

This geometric model will be combined with the physical model in the next section. A cloud removal method will then be generated.

C. Cloud Removal Model

The proposed cloud removal model ST-SMA is achieved by combining the physical analysis of the cloud effect and the

Scene	Path/Row	Acquisition date	Sensor	Cloud cover type
1	90/85	2013-9-9	OLI	Presence of moderate cloud, relatively thin with several patches of thick cloud.
2	96/72	2014-1-26	OLI	Thin cloud distributed over river, forest and grassland.
3	89/83	2014-3-13	OLI	Relatively thick cloud cover in left area of image within large region of water body.
4	193/14	2013-8-26	Hyperion	Wide thin cloud cover over Lulea urban region and Lulealven river.

geometric description of the mixed reflectance from the ground as detailed below. If we substitute (13) into (12), we have

$$\mathbf{x} = (1 - \Gamma) \sum_{m=1}^{M} a_m \mathbf{s_m} + \Gamma \mathbf{s_c} + \mathbf{e} \qquad (14)$$

$$\text{s.t.} \quad \sum_{m=1}^{M} a_m = 1, \, a_m \geq 0, \quad 0 \leq \Gamma \leq 1. \qquad (15)$$

If we let $a_{M+1} = \Gamma/(1 - \Gamma)$ and $\mathbf{s_{M+1}} = \mathbf{s_c}$, (14) becomes

$$\mathbf{x} = (1 - \Gamma) \sum_{m=1}^{M+1} a_m \mathbf{s_m} + \mathbf{e}. \qquad (16)$$

Then if we let $b_m = (1 - \Gamma)a_m$, (16) becomes

$$\mathbf{x} = \sum_{m=1}^{M+1} b_m \mathbf{s_m} + \mathbf{e} \qquad (17)$$

$$\text{s.t.} \quad \sum_{m=1}^{M} b_m = 1 - \Gamma, 0 \leq b_m \leq \Gamma, 0 \leq \Gamma \leq 1. \qquad (18)$$

We can see that (17) has a form similar to the standard form of LSMM, but with different constraints. Also, in the proposed model we can interpret cloud as one of the endmember classes. Then the new endmember signature matrix can be considered as $[\mathbf{s_1}, \mathbf{s_2}, \ldots, \mathbf{s_M}, \mathbf{s_c}]$. Γ can be regarded as cloud fractional abundance. In the aforementioned set of simultaneous equations (L equations), there are $M + 1$ unknowns, i.e., M fractions for M endmembers, plus the cloud thickness factor Γ. As long as $L > M + 1$, all the unknowns can be estimated with the new constraints. After Γ is estimated, the cloud effect can be removed as follows for $0 <= \Gamma < 1$:

$$\mathbf{x}^* = \frac{1}{1 - \Gamma} (\mathbf{x} - \Gamma \mathbf{s_c}) \qquad (19)$$

where $\mathbf{x}^*$ is the corrected image after cloud removal. $\Gamma \mathbf{s_c}$ is a side product which represents various cloud contributions depending on their thickness at a subpixel level. This cloud retrieval result provides more detailed information than a binary mask file for cloud detection only. Specifically, cloud detection is achieved in the proposed cloud removal model after the cloud abundance is obtained. The fractional maps of the other materials are intermediate products as well. However, we mainly focus on cloud thickness in this paper.

The correction fails when $\Gamma = 1$. If $\Gamma = 1$, according to (14), $\mathbf{x} \approx \mathbf{s_c}$. Applying (19), $\mathbf{x}^* = 0$. This refers to the case of opaque clouds, which means that the underlying ground signal has been completely blocked. In this situation, reconstruction

methods can be applied, e.g., by using multitemporal images to estimate the data of the blocked pixels [45]–[48]. In this paper, we focus on transparent thin cloud cases only.

IV. EXPERIMENTAL RESULTS

A. Study Area and Data

To test the performance of the ST-SMA method, multispectral and hyperspectral images from the Landsat 8 OLI and EO-1 Hyperion, respectively, were used in our experiments. The details of the experimental images are summarized in Table I.

1) Landsat 8 OLI Data: Landsat 8 OLI multispectral images contain eight spectral bands with a spatial resolution of 30 m. The study areas selected from OLI were in Australia encompassing three typical landscapes with different types of clouds.

Validation of the performance of a cloud removal approach is not an easy task since there is no ground reference in the simultaneous atmospheric conditions. Fortunately, OLI captures a new spectral band (Band 9) at wavelengths ranging from 1.36 μm to 1.38 μm for detecting cirrus clouds. This narrow band has a strong ability to identify water vapor absorption and cirrus signal scattering [12], [49]. Cirrus cloud will appear bright in this band while sunlight reflected from the land's surface will be entirely absorbed. Hence, this band is advantageous for cirrus cloud detection. This cirrus band with center wavelengths at 1.375 μm was used to validate the cloud detection results in this study.

2) EO-1 Hyperion Data: The Hyperion hyperspectral data were collected by the EO-1 satellite which was launched in November 2000. Hyperion images contain 242 spectral bands with wavelengths from 400 nm to 2500 nm with 30-m spatial resolution. The first 70 bands cover the visible/near-infrared region, and the bands from 71 to 242 cover the shortwave-infrared region. Level 1R data downloaded from the USGS website (http://earthexplorer.usgs.gov/) gave radiometrically corrected images which were used in this study. A subset of the Hyperion data with 122 bands was kept after calibration and noisy band removal. The Hyperion test data were selected in the Lulea region in Sweden as scene 4 showed in Table I. The water area is Lulealven river in the east of Sweden.

We also selected cloud free images from the closest date to each scene from the USGS website (http://earthexplorer.usgs.gov/) and used them to assess the quality of the corrected data. We assume that little change happened in the period between the two acquisition dates and only the atmospheric condition was different between the cloudy and cloud-free images. The images tested in the study were of size 400×400 pixels for the OLI image and 1000×256 pixels for Hyperion data. Image normalization was performed by converting the raw digital number to top-of-atmosphere reflectance ranging from 0 to 1.
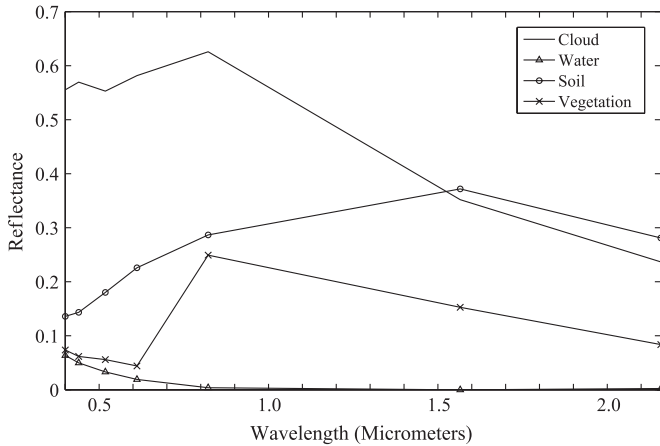
Fig. 4. Spectral reflectance of endmembers in scene 1.

In general, it can reduce scene-to-scene variability. Within the data set, the shape of the solar spectrum was compensated to enhance the spectral differences between the cloud spectrum and other endmembers [50].

B. Cloud Thickness Extraction

Cloud thickness can be obtained by solving the unmixing problems in our cloud removal model. Due to different atmospheric conditions, solar angles, and cloud cover in different dates and locations, the cloud endmember was extracted from each cloudy image separately based on (10).

Fig. 4 illustrates the spectral reflectance of the cloud endmember (solid line) for scene 1. Following the selection of the cloud endmember, the other three endmembers were retrieved from land ground pixels using the VCA method [43]. VCA is an EEA which assumes the presence of pure pixels, and it is effective and applicable for our cases. In the VCA algorithm, endmembers are presented as the vertices of a simplex and their selection are achieved by iteratively projecting to orthogonal directions in a subspace projection of an initially determined endmember. The iterative process stops when a predefined number of endmembers is extracted. Fig. 4 shows the spectra of three distinct materials identified in scene 1. Accordingly, ten endmembers were extracted for the Hyperion scene 4. Cloud thickness Γ was obtained by solving (14) with the constraints as discussed in the previous section.

Cloud detection and removal were also performed using the HOT method [21]. Fig. 5 shows the original image, cloud detection results using the proposed method ST-SMA and the HOT method, and the corresponding cirrus band for the OLI scenes. The value of a pixel in the cloud detected image represents the thickness of cloud. We can see that HOT method provides good performance for scene 1 as shown in Fig. 5(c), but poorer performance for scenes 2 and 3 as shown in Fig. 5(g) and (k) where some background features appear, especially for large water bodies. Our method performs much better as shown in Fig. 5(d), (h), and (l). For the purpose of quantitatively validating the cloud detection results, scatterplots of the cloud detection results versus the cirrus band were generated and are shown in Fig. 7. The correlation coefficient between cloud thickness derived by the ST-SMA and the cirrus band data is 0.939, 0.801, and 0.939 for the three scenes, respectively,

whereas the correlation coefficient obtained by the HOT methods was 0.844, 0.781, and 0.721, respectively. This quantitative assessment also shows that the proposed method performs better than the HOT method for all the OLI scenes.

C. Cloud Correction Results

In this set of experiments we assess the quality of the corrected images by comparing it with reference images. (19) was applied to conduct the cloud removal for the four scenes using the cloud thickness estimated in the earlier step. Figs. 6 and 8 show the original images, the reference images, and the corrected images of OLI and Hyperion data, respectively. From a qualitative point of view, we can see from Fig. 6 that the proposed method works effectively for various backgrounds with different land covers and cloud types. When the cloud is relatively thick and the ground cover underneath the cloud has high reflectance, the HOT method over-corrected the images while our method could clearly restore the land features. Fig. 8 reveals a good visual result of the corrected Hyperion image using ST-SMA method. The thin clouds over the whole scene have been effectively removed. The execution time of the proposed method on an EO-1 Hyperion subset is less than one second for 1000 pixels with 122 bands on a PC with an Intel® Core i7-3770 CPU at 3.4 GHz, 64-bit Operating System. The total execution time for the full scene is about 5 min, which can be reduced if a better CPU and code optimized for speed is used.

A comparison of spectral profile from cloudy, corrected, and reference images is selected as another validation approach. Fig. 9 depicts the spectral profiles of vegetation, water, and soil areas before and after the correction using the ST-SMA and HOT methods, respectively, as well as the reference data for scene 1. These profiles show the mean values of 10 randomly selected regions in the cloud cover areas. We can see that the spectral profile of corrected image by ST-SMA has a more similar shape with the profile from the reference image when compared with the HOT method. Fig. 9 also illustrates that the ST-SMA cloud removal method does not change the spectral properties of original data.

We also applied the spectral angle mapper (SAM) [51] to quantitatively evaluate the similarity between the cloudy (or corrected) spectra and the reference spectra. If a spectrum $s(n), n = 1, 2, \ldots, N$ is treated as a vector $\mathbf{s}$ in which N is the number of bands. The SAM measures the spectral angle between $\mathbf{s_i}$ and $\mathbf{s_j}$ by calculating the *arccosine* of the normalized dot product of the spectra using

$$\alpha = \cos^{-1}\left(\frac{\mathbf{s_i} \cdot \mathbf{s_j}}{\|\mathbf{s_i}\| \|\mathbf{s_j}\|}\right)$$

$$= \cos^{-1}\left(\frac{\sum_{n=1}^{N} s_i(n)s_j(n)}{\left(\sum_{n=1}^{N} s_i^2(n)\right)^{\frac{1}{2}}\left(\sum_{n=1}^{N} s_j^2(n)\right)^{\frac{1}{2}}}\right). \tag{20}$$

Smaller angles indicate higher similarity, although the magnitude of the vectors can be different. The SAM results of Fig. 9(a) were 0.254 (cloudy versus reference), 0.136 (HOT versus reference), and 0.086 (ST-SMA versus reference),
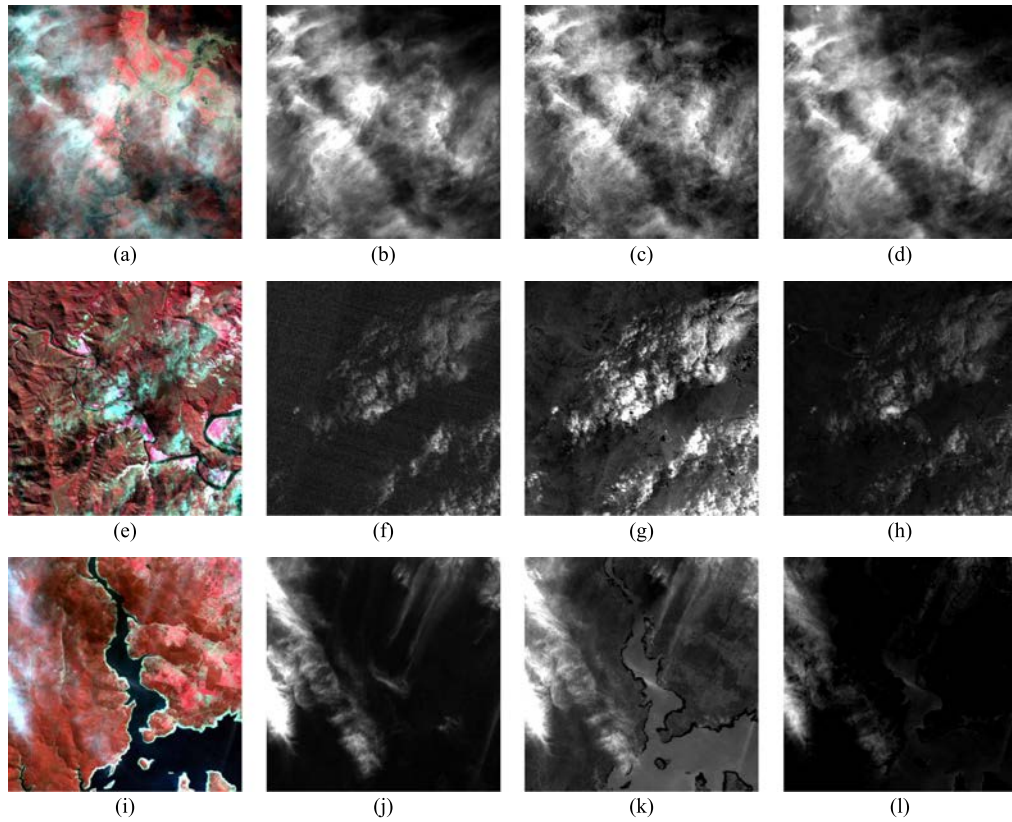
Fig. 5. Comparison of cloud detection results for the OLI data. (a) Original image-scene 1. (b) Cirrus band-scene 1. (c) HOT results-scene 1. (d) ST-SMA results-scene 1. (e) Original image-scene 2. (f) Cirrus band-scene 2. (g) HOT results-scene 2. (h) ST-SMA results-scene 2. (i) Original image-scene 3. (j) Cirrus band-scene 3. (k) HOT results-scene 3. (l) ST-SMA results-scene 3.
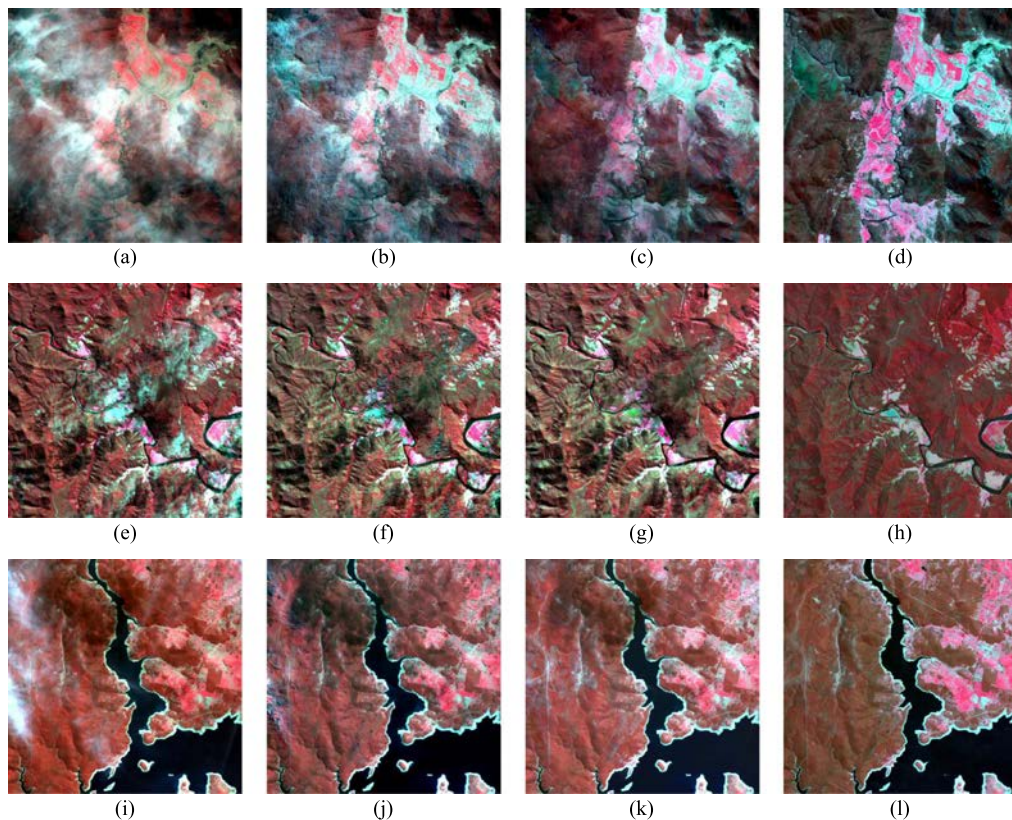

Fig. 6. Cloud removal results and reference images of OLI data (R = band 5, G = band 4, B = band 3). (a) Cloudy image-scene 1. (b) HOT-scene 1. (c) ST-SMA-scene 1. (d) Reference image-scene 1. (e) Cloudy image-scene 2. (f) HOT-scene 2. (g) ST-SMA-scene 2. (h) Reference image-scene 2. (i) Cloudy image-scene 3. (j) HOT-scene 3. (k) ST-SMA-scene 3. (l) Reference image-scene 3.
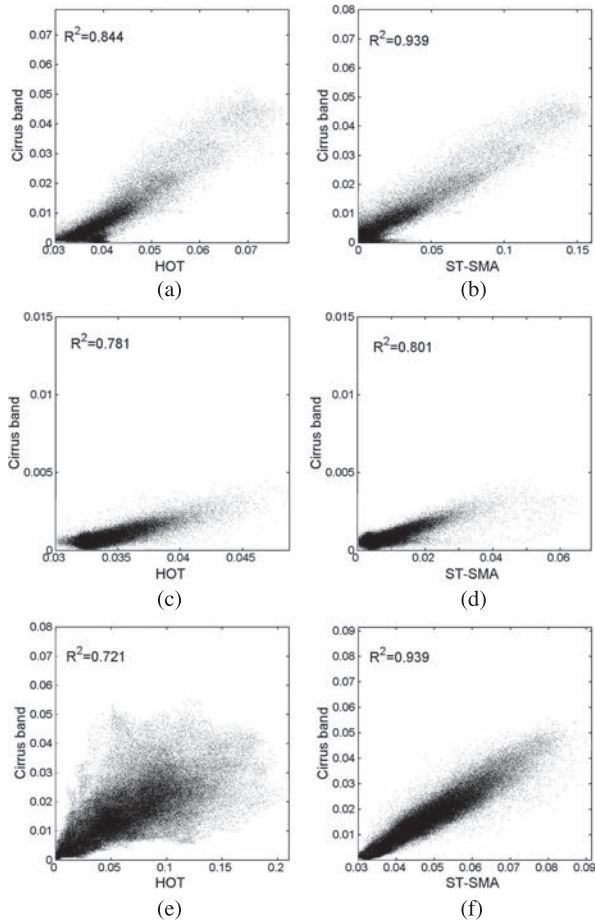
Fig. 7. Scatterplots of HOT results and ST-SMA results versus cirrus band values for the multispectral scenes. (a) Scene 1. (b) Scene 1. (c) Scene 2. (d) Scene 2. (e) Scene 3. (f) Scene 3.
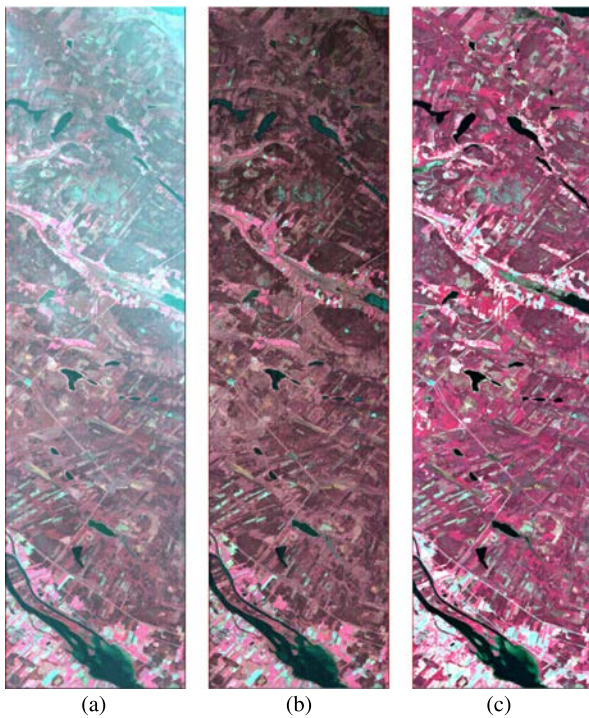

Fig. 8. Cloud removal results and reference images of Hyperion data (R = band 49, G = band 29, B = band 20). (a) Cloudy image-scene 4. (b) ST-SMA-scene 4. (c) Reference image-scene 4.
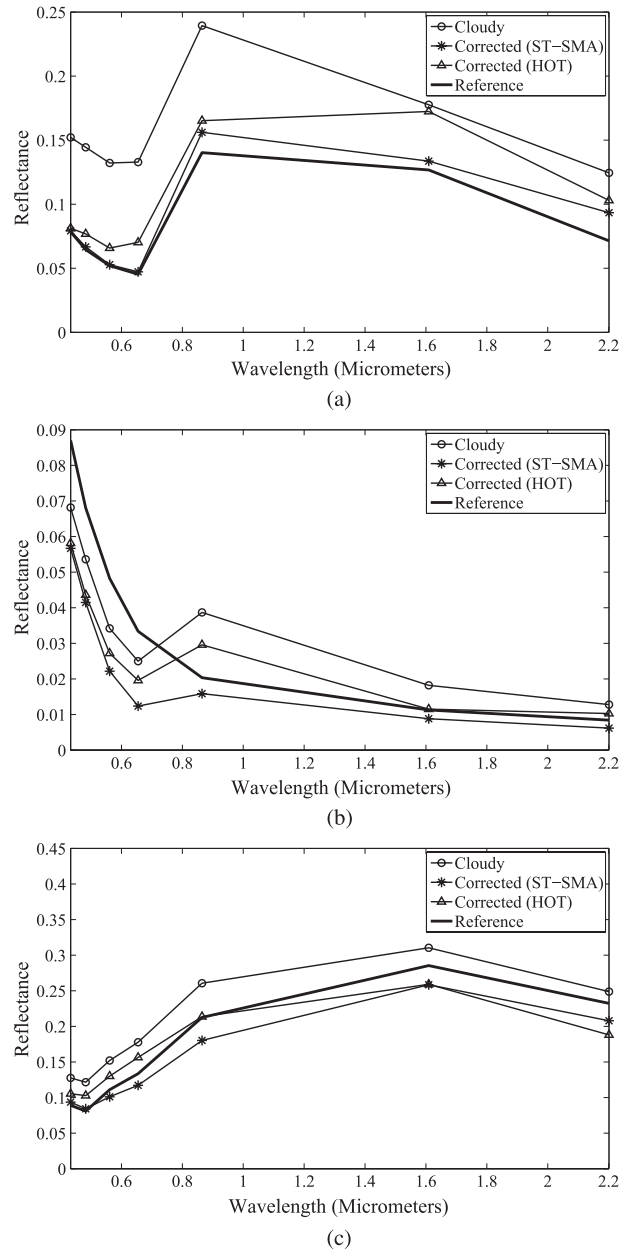

Fig. 9. Spectral profile of mean value from ten polygon samples in the cloud cover areas for cloudy, corrected and reference images for scene 1. (a) Vegetation. (b) Water. (c) Soil.

respectively. Accordingly, results of Fig. 9(b) and (c) are 0.242, 0.211, 0.156 and 0.136, 0.103, 0.05, respectively. The lowest SAM values, 0.086, 0.156, and 0.05, indicate that the shape of the corrected spectra using ST-SMA is the closest to the reference spectra.

Table II provides detailed R^2 results of the cloudy and corrected images versus reference images, band by band, for the three OLI scenes. We can see that the R^2 value of corrected versus reference images is much higher than cloudy versus reference images in coastal aerosol and visible bands. This is due to the strong effects of cloud cover in these bands. In near in-frared and shortwave infrared bands, the R^2 value of corrected versus reference images improved slightly since the cloudy and reference images already have relatively high agreement. Between the two methods implemented on OLI images, the

TABLE II
LINEAR REGRESSION MODEL OF CLOUDY AND CORRECTED
IMAGES BY THE ST-SMA AND HOT METHODS VERSUS
REFERENCE IMAGES OVER ALL CLOUDY PIXELS

| | | R^2 | | | | | | |
		Band 1	Band 2	Band 3	Band 4	Band 5	Band 6	Band 7
	Cloudy	0.233	0.271	0.383	0.434	0.652	0.851	0.805
Scene 1	HOT	0.537	0.558	0.602	0.723	0.739	0.863	0.875
	ST-SMA	**0.798**	**0.834**	**0.856**	**0.845**	**0.792**	**0.874**	**0.896**
	Cloudy	0.281	0.383	0.611	0.752	0.881	0.892	0.896
Scene 2	HOT	0.781	0.824	0.879	0.886	0.899	0.912	0.923
	ST-SMA	**0.802**	**0.844**	**0.896**	**0.913**	**0.925**	**0.928**	**0.935**
	Cloudy	0.366	0.424	0.648	0.566	0.645	0.575	0.631
Scene 3	HOT	0.456	0.523	0.712	0.635	0.718	0.625	0.712
	ST-SMA	**0.468**	**0.587**	**0.715**	**0.641**	**0.728**	**0.749**	**0.788**

ST-SMA method outperforms the HOT method consistently. The normalized difference vegetation indices (NDVI) of the cloudy and corrected Hyperion images were also compared. From the scatterplots in Fig. 10, the corrected image using ST-SMA method has higher R^2 vaule (0.718) than the cloudy image (0.456). The corrected images are expected to be valuable for classification and target detection.

While snow can be confused with clouds in the visible bands, they have different spectral profiles in other bands [52]. In our proposed cloud removal method, snow is treated as a unique endmember like other ground cover types. Fig. 11 shows the cloud removal results of an image with both snow and cloud cover. Fig. 11(a) and (b) are the original image and the corrected image, respectively. We can see that the cloud effect is removed, while snow is still present.

V. DISCUSSIONS AND CONCLUSIONS

In this paper, we have developed a new method, called ST-SMA, for cloud thickness detection and cloud removal in optical remote sensing imagery. ST-SMA makes joint use of atmospheric scattering theory and linear spectral mixture analysis to describe the effects of cloud on the reflectance from underlying land. The approach is based on the assumption that there is a linear relationship between cloud thickness and spectral reflectance. Energy absorption is also considered in the solar radiation propagation model. Cloud saturation is not considered in this study given that we focus on thin cloud removal. A concept of pure cloud is introduced in this paper, and we propose to extract a cloud spectrum by searching for the pixels with the maximum total energy in all the spectral bands in each cloud-affected image. A modified version of fully constrained linear spectral unmixing was applied to estimate cloud thickness, which is equivalent to cloud abundance. Cloud thickness is presented for each pixel instead of binary masking only. This represents a novel contribution for cloud detection and removal by combining physical modeling and mixture analysis. The proposed method has no requirement for meteorological data and does not rely on reference images.

The screening results of multispectral data were visually and quantitatively compared with the cirrus band of the Landsat OLI sensor. Validation of the cloud removal algorithm was conducted for OLI and Hyperion data by comparing corrected images with reference images through scatter plots and R^2 values and spectral similarity evaluation with SAM. The HOT method was also implemented in the experiments. The testing results demonstrate that our method ST-SMA provides better
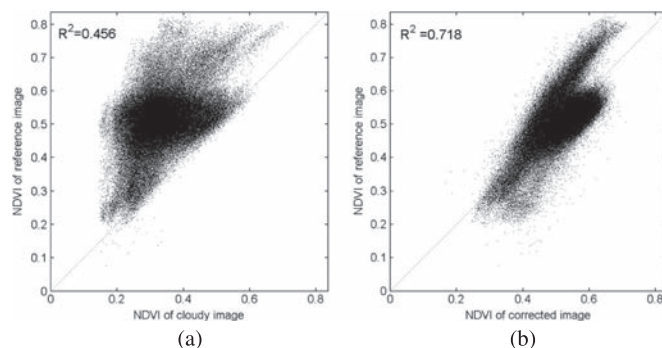

Fig. 10. Scatterplots of NDVI values for scene 4 (NIR = band 49, RED = band 29). (a) The cloudy image versus the reference image and (b) the corrected image versus the reference image.
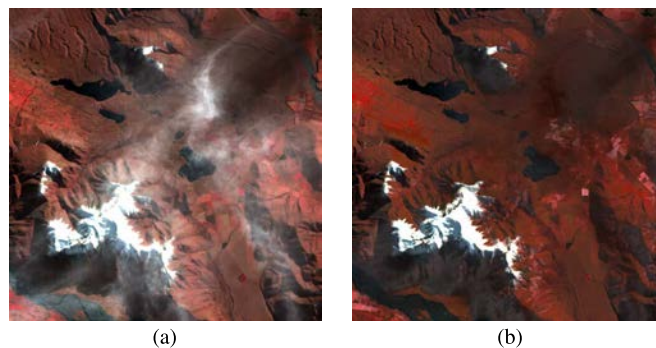

Fig. 11. Cloud removal results of cloudy image with both snow and cloud cover. (a) Cloudy image with snow. (b) Corrected image.

performance than the HOT method and can provide cloud free images with high quality.

The cloud removal performance is sensitive to some parameters in the proposed method. First and foremost, the cloud endmember should be selected in regions containing the thickest cloud. This is not a difficult issue in practice since it is very easy to find these areas in optical images. Second, the number of endmembers needs to be smaller than the number of spectral bands to make the least squares solution reliable. For correction of Landsat 8 images, the proposed method is mainly suitable for simple landscapes, containing three or four endmember classes only. For complicated scenes, such as urban areas, the ST-SMA method can be applied to hyperspectral images where the number of bands can be over two hundred. Alternatively, the pixel-adapted subset of endmembers can be used in unmixing. The conventional approach is to find all the endmembers present in the whole image and unmix each pixel into the complete set of endmembers. More efficient methods have been developed to estimate a subset of endmembers for which individual pixels are associated with first, and the unmixing is then conducted adaptively for each pixel [53], [54]. In this way, the number of potential endmembers for each particular pixel is often reduced to 3 or 4, and this allows, to some extent, the use of spectral unmixing techniques with multispectral data. Extra computational load is introduced by the nonlinear least squares problem involved in ST-SMA; however, it is not a serious issue as cloud removal is an off-board post-processing task. Cloud shadow is difficult to model and it is not addressed in this paper since it is not as relevant when we focus on thin cloud contaminated image restoration.

In our future work, the cirrus band will be considered to assist with the cloud detection. Wider testing will be conducted, for example, on the case of cloud contamination over snow, which presents relevant challenges. The corrected images will also be further processed for various applications.

REFERENCES

[1] J. R. Irons, J. L. Dwyer, and J. A. Barsi, "The next Landsat satellite: The Landsat data continuity mission," *Remote Sens. Environ.*, vol. 122, pp. 11–21, Jul. 2012.

[2] J. Ju and D. P. Roy, "The availability of cloud-free Landsat ETM+ data over the conterminous united states and globally," *Remote Sens. Environ.*, vol. 112, no. 3, pp. 1196–1211, Mar. 2008.

[3] X. Lan, L. Zhang, H. Shen, Q. Yuan, and H. Li, "Single image haze removal considering sensor blur and noise," *EURASIP J. Adv. Signal Process.*, vol. 2013, no. 1, p. 86, Dec. 2013.

[4] D. Hadjimitsis, C. Clayton, and V. Hope, "An assessment of the effectiveness of atmospheric correction algorithms through the remote sensing of some reservoirs," *Int. J. Remote Sens.*, vol. 25, no. 18, pp. 3651–3674, Sep. 2004.

[5] Q. Cheng, H. Shen, L. Zhang, Q. Yuan, and C. Zeng, "Cloud removal for remotely sensed images by similar pixel replacement guided with a spatio-temporal MRF model," *ISPRS J. Photogramm. Remote Sens.*, vol. 92, pp. 54–68, Jun. 2014.

[6] X. Li *et al.*, "Recovering quantitative remote sensing products contaminated by thick clouds and shadows using multitemporal dictionary learning," *IEEE Trans. Geosci. Remote Sens.*, vol. 52, no. 11, pp. 7086–7098, Nov. 2014.

[7] R. R. Irish, "Landsat 7 automatic cloud cover assessment," in *Proc. AeroSense*, 2000, pp. 348–355.

[8] R. R. Irish, J. L. Barker, S. N. Goward, and T. Arvidson, "Characterization of the Landsat-7 ETM+ Automated Cloud-Cover Assessment (ACCA) algorithm," *Photogramm. Eng. Remote Sens.*, vol. 72, no. 10, pp. 1179–1188, Oct. 2006.

[9] Z. Zhu and C. E. Woodcock, "Object-based cloud and cloud shadow detection in Landsat imagery," *Remote Sens. Environ.*, vol. 118, pp. 83–94, Mar. 2012.

[10] C. Ji, "Haze reduction from the visible bands of Landsat TM and ETM+ images over a shallow water reef environment," *Remote Sens. Environ.*, vol. 112, no. 4, pp. 1773–1783, Apr. 2008.

[11] C. Liu, J. Hu, Y. Lin, S. Wu, and W. Huang, "Haze detection, perfection and removal for high spatial resolution satellite imagery," *Int. J. Remote Sens.*, vol. 32, no. 23, pp. 8685–8697, Dec. 2011.

[12] B. C. Gao, A. F. Goetz, and W. J. Wiscombe, "Cirrus cloud detection from airborne imaging spectrometer data using the 1.38 μm water vapor band," *Geophys. Res. Lett.*, vol. 20, no. 4, pp. 301–304, Feb. 1993.

[13] B. C. Gao, Y. J. Kaufman, W. Han, and W. J. Wiscombe, "Correction of thin cirrus path radiances in the 0.4–1.0 μm spectral region using the sensitive 1.375 μm cirrus detecting channel," *J. Geophys. Res., Atmos.*, vol. 103, no. D24, pp. 32 169–32 176, Dec. 1998.

[14] O. Hagolle, M. Huc, D. V. Pascual, and G. Dedieu, "A multitemporal method for cloud detection, applied to FORMOSAT-2, VENμS, LANDSAT and SENTINEL-2 images," *Remote Sens. Environ.*, vol. 114, no. 8, pp. 1747–1755, Aug. 2010.

[15] S. Gabarda and G. Cristbal, "Cloud covering denoising through image fusion," *Image Vis. Comput.*, vol. 25, no. 5, pp. 523–530, May 2007.

[16] H. Li, L. Zhang, H. Shen, and P. Li, "A variational gradient-based fusion method for visible and SWIR imagery," *Photogramm. Eng. Remote Sens.*, vol. 78, no. 9, pp. 947–958, Sep. 2012.

[17] J. A. T. Arriaza, F. G. Rojas, M. P. López, and M. Cantón, "An automatic cloud-masking system using backpro neural nets for AVHRR scenes," *IEEE Trans. Geosci. Remote Sens.*, vol. 41, no. 4, pp. 826–831, Apr. 2003.

[18] F. Murtagh, D. Barreto, and J. Marcello, "Decision boundaries using bayes factors: The case of cloud masks," *IEEE Trans. Geosci. Remote Sens.*, vol. 41, no. 12, pp. 2952–2958, Dec. 2003.

[19] P. S. Chavez Jr., "An improved dark-object subtraction technique for atmospheric scattering correction of multispectral data," *Remote Sens. Environ.*, vol. 24, no. 3, pp. 459–479, Apr. 1988.

[20] P. S. Chavez, "Image-based atmospheric corrections-revisited and improved," *Photogramm. Eng. Remote Sens.*, vol. 62, no. 9, pp. 1025–1035, Sep. 1996.

[21] Y. Zhang, B. Guindon, and J. Cihlar, "An image transform to characterize and compensate for spatial variations in thin cloud contamination of Landsat images," *Remote Sens. Environ.*, vol. 82, no. 2/3, pp. 173–187, Oct. 2002.

[22] Y. Zhang and B. Guindon, "Quantitative assessment of a haze suppression methodology for satellite imagery: Effect on land cover classification performance," *IEEE Trans. Geosci. Remote Sens.*, vol. 41, no. 5, pp. 1082–1089, May 2003.

[23] H. Li, L. Zhang, and H. Shen, "A principal component based haze masking method for visible images," *IEEE Geosci. Remote Sens. Lett.*, vol. 11, no. 5, pp. 975–979, May 2014.

[24] O. Mitchell, E. Delp, and P. Chen, "Filtering to remove cloud cover in satellite imagery," *IEEE Trans. Geosci. Remote Sens.*, vol. GE-15, no. 3, pp. 137–141, Jul. 1977.

[25] Y. Kechu and W. Wentao, "On removing cloud interference in remote-sensing images," *J. Electron. (China)*, vol. 1, no. 1, pp. 18–27, Jan. 1984.

[26] B. Chanda and D. D. Majumder, "An iterative algorithm for removing the effect of thin cloud cover from LANDSAT imagery," *Math. Geol.*, vol. 23, no. 6, pp. 853–860, Jul. 1991.

[27] H. Shen, H. Li, Y. Qian, L. Zhang, and Q. Yuan, "An effective thin cloud removal procedure for visible remote sensing images," *ISPRS J. Photogramm. Remote Sens.*, vol. 96, pp. 224–235, Oct. 2014.

[28] Z. Liu and B. R. Hunt, "A new approach to removing cloud cover from satellite imagery," *Comput. Vis. Graph. Image Process.*, vol. 25, no. 2, pp. 252–256, Feb. 1984.

[29] Q. Meng, B. E. Borders, C. J. Cieszewski, and M. Madden, "Closest spectral fit for removing clouds and cloud shadows," *Photogramm. Eng. Remote Sens.*, vol. 75, no. 5, pp. 569–576, May 2009.

[30] L. Gómez-Chova, G. Camps-Valls, J. Calpe-Maravilla, L. Guanter, and J. Moreno, "Cloud-screening algorithm for ENVISAT/MERIS multispectral images," *IEEE Trans. Geosci. Remote Sens.*, vol. 45, no. 12, pp. 4105–4118, Dec. 2007.

[31] D.-C. Tseng, H.-T. Tseng, and C.-L. Chien, "Automatic cloud removal from multi-temporal SPOT images," *Appl. Math. Comput.*, vol. 205, no. 2, pp. 584–600, Nov. 2008.

[32] Y. Gu *et al.*, "Multiple-kernel learning-based unmixing algorithm for estimation of cloud fractions with MODIS and CloudSat data," in *Proc. IEEE IGARSS*, 2012, pp. 1785–1788.

[33] N. Keshava and J. F. Mustard, "Spectral unmixing," *IEEE Signal Process. Mag.*, vol. 19, no. 1, pp. 44–57, Jan. 2002.

[34] C. Quintano, A. Fernndez-Manso, Y. E. Shimabukuro, and G. Pereira, "Spectral unmixing," *Int. J. Remote Sens.*, vol. 33, no. 17, pp. 5307–5340, Sep. 2012.

[35] J. M. Bioucas-Dias *et al.*, "Hyperspectral unmixing overview: Geometrical, statistical, and sparse regression-based approaches," *IEEE J. Sel. Topics Appl. Earth Observ. Remote Sens.*, vol. 5, no. 2, pp. 354–379, Apr. 2012.

[36] D. C. Heinz and C.-I. Chang, "Fully constrained least squares linear spectral mixture analysis method for material quantification in hyperspectral imagery," *IEEE Trans. Geosci. Remote Sens.*, vol. 39, no. 3, pp. 529–545, Mar. 2001.

[37] G. L. Stephens and C. D. Kummerow, "The remote sensing of clouds and precipitation from space: A review," *J. Atmos. Sci.*, vol. 64, no. 11, pp. 3742–3765, Nov. 2007.

[38] B. C. Kindel, P. Pilewskie, K. S. Schmidt, O. Coddington, and M. D. King, "Solar spectral absorption by marine stratus clouds: Measurements and modeling," *J. Geophys. Res., Atmos.*, vol. 116, no. D10, May 2011, Art. ID. D10203.

[39] T. M. Lillesand, R. W. Kiefer, and J. W. Chipman, *Remote Sensing and Image Interpretation.* Hoboken, NJ, USA: Wiley, 2004.

[40] J. W. Boardman, F. A. Kruse, and R. O. Green, "Mapping target signatures via partial unmixing of AVIRIS data," in *Proc. Summaries 5th JPL Airborne Earth Sci. Workshop*, Pasadena, CA, USA, 1995, pp. 23–26.

[41] C.-I. Chang and A. Plaza, "A fast iterative algorithm for implementation of pixel purity index," *IEEE Geosci. Remote Sens. Lett.*, vol. 3, no. 1, pp. 63–67, Jan. 2006.

[42] M. E. Winter, "N-FINDR: An algorithm for fast autonomous spectral endmember determination in hyperspectral data," in *Proc. SPIE Int. Symp. Opt. Sci., Eng., Instrum.*, 1999, pp. 266–275.

[43] J. M. Nascimento and J. M. Bioucas Dias, "Vertex component analysis: A fast algorithm to unmix hyperspectral data," *IEEE Trans. Geosci. Remote Sens.*, vol. 43, no. 4, pp. 898–910, Apr. 2005.

[44] M. Lidan and Q. Hairong, "Endmember extraction from highly mixed data using minimum volume constrained nonnegative matrix factorization," *IEEE Trans. Geosci. Remote Sens.*, vol. 45, no. 3, pp. 765–777, Mar. 2007.

[45] C.-H. Lin, K.-H. Lai, Z.-B. Chen, and J.-Y. Chen, "Patch-based information reconstruction of cloud-contaminated multitemporal images," *IEEE Trans. Geosci. Remote Sens.*, vol. 52, no. 1, pp. 163–174, Jan. 2014.

[46] C.-H. Lin, P.-H. Tsai, K.-H. Lai, and J.-Y. Chen, "Cloud removal from multitemporal satellite images using information cloning," *IEEE Trans. Geosci. Remote Sens.*, vol. 51, no. 1, pp. 232–241, Jan. 2013.

[47] A. Maalouf, P. Carré, B. Augereau, and C. Fernandez-Maloigne, "A bandelet-based inpainting technique for clouds removal from remotely sensed images," *IEEE Trans. Geosci. Remote Sens.*, vol. 47, no. 7, pp. 2363–2371, Jul. 2009.

[48] F. Melgani, "Contextual reconstruction of cloud-contaminated multitemporal multispectral images," *IEEE Trans. Geosci. Remote Sens.*, vol. 44, no. 2, pp. 442–455, Feb. 2006.

[49] K. Meyer, P. Yang, and B. C. Gao, "Optical thickness of tropical cirrus clouds derived from the MODIS 0.66 and 1.375 μm channels," *IEEE Trans. Geosci. Remote Sens.*, vol. 42, no. 4, pp. 833–841, Apr. 2004.

[50] G. Chander, B. L. Markham, and D. L. Helder, "Summary of current radiometric calibration coefficients for Landsat MSS, TM, ETM+, and EO-1 ALI sensors," *Remote Sens. Environ.*, vol. 113, no. 5, pp. 893–903, May 2009.

[51] R. Yuhas, A. Goetz, and J. Boardman, "Discrimination among semi-arid landscape endmembers using the spectral angle mapper(SAM) algorithm," in *Proc. Summaries 3rd Annu. JPL Airborne Geosci. Workshop*, 1992, vol. 1, pp. 147–149.

[52] J. Krijger, I. Aben, and H. Schrijver, "Distinction between clouds and ice/snow covered surfaces in the identification of cloud-free observations using SCIAMACHY PMDS," *Atmos. Chem. Phys.*, vol. 5, no. 10, pp. 2729–2738, Oct. 2005.

[53] X. Jia, C. Dey, D. Fraser, L. Lymburner, and A. Lewis, "Controlled spectral unmixing using extended support vector machines," in *Proc. 2nd WHISPERS*, 2010, pp. 1–4.

[54] A. Villa, J. Chanussot, J. A. Benediktsson, and C. Jutten, "Spectral unmixing for the classification of hyperspectral images at a finer spatial resolution," *IEEE J. Sel. Topics Signal Process.*, vol. 5, no. 3, pp. 521–533, Jun. 2011.

Antonio J. Plaza (M'05–SM'07–F'15) received the bachelor, M.Sc., and Ph.D. degrees from the University of Extremadura, Extremadura, Spain, in 1997, 1999, and 2002, respectively, all in computer engineering.

He is an Associate Professor (with accreditation for Full Professor) with the Department of Technology of Computers and Communications, University of Extremadura, where he is the Head of the Hyperspectral Computing Laboratory (HyperComp). From 2007 to 2011, he was the Coordinator of the Hyperspectral Imaging Network, a European project with total funding of 2.8 million euros. He authored more than 400 publications, including 126 JCR journal papers (78 in IEEE journals), 20 book chapters, and over 240 peer-reviewed conference proceeding papers (94 in IEEE conferences). He has edited the book *High-Performance Computing in Remote Sensing* (CRC Press/Taylor and Francis) (the first book on this topic in the published literature) and guest edited eight special issues on hyperspectral remote sensing for different journals.

Dr. Plaza served as an Associate Editor for the IEEE TRANSACTIONS ON GEOSCIENCE AND REMOTE SENSING from 2007 to 2012. He is a Guest Editor of seven special issues on JCR journals (three in IEEE journals). He was a member of the Editorial Board of the IEEE GEOSCIENCE AND REMOTE SENSING NEWSLETTER from 2011 to 2012 and a member of the steering committee of the IEEE JOURNAL OF SELECTED TOPICS IN APPLIED EARTH OBSERVATIONS AND REMOTE SENSING in 2012. He is also an Associate Editor for IEEE ACCESS and the IEEE GEOSCIENCE AND REMOTE SENSING MAGAZINE. He is currently serving as the Editor-in-Chief of the IEEE TRANSACTIONS ON GEOSCIENCE AND REMOTE SENSING (since January 2013). He served as the Chair of the 2011 IEEE Workshop on Hyperspectral Image and Signal Processing: Evolution in Remote Sensing. He served as the Director of Education Activities for the IEEE Geoscience and Remote Sensing Society (GRSS) from 2011 to 2012, and is currently serving as President of the Spanish Chapter of IEEE GRSS (since November 2012). He received the recognition of Best Reviewers of the IEEE GEOSCIENCE AND REMOTE SENSING LETTERS in 2009 and of Best Reviewers of the IEEE TRANSACTIONS ON GEOSCIENCE AND REMOTE SENSING in 2010.

Meng Xu (S'13) received the B.S. and M.S. degrees in electrical engineering from the Ocean University of China, Qingdao, China, in 2011 and 2013, respectively. She is currently working toward the Ph.D. degree in the School of Engineering and Information Technology, University of New South Wales, Canberra, ACT, Australia.

Her research interests include cloud removal and remote sensing image processing.

Xiuping Jia (M'93–SM'03) received the B.Eng. degree from the Beijing University of Posts and Telecommunications, Beijing, China, in 1982 and the Ph.D. degree in electrical engineering from The University of New South Wales, Australia, in 1996.

Since 1988, she has been with the School of Information Technology and Electrical Engineering, The University of New South Wales, Canberra, Australia, where she is currently a Senior Lecturer. She is also a Guest Professor with Harbin Engineering University, China, and an Adjunct Researcher at China National Engineering Research Center for Information Technology in Agriculture. She is the coauthor of the remote sensing textbook titled *Remote Sensing Digital Image Analysis* [Springer-Verlag, 3rd (1999) and 4th eds. (2006)]. Her research interests include remote sensing, imaging spectrometry and spatial data analysis.

Dr. Xia is an Editor of the *Annals of GIS* and an Associate Editor of the IEEE TRANSACTIONS ON GEOSCIENCE AND REMOTE SENSING.

Mark Pickering (S'92–M'95) was born in Biloela, Australia, in 1966. He received the B.Eng. degree from the Capricornia Institute of Advanced Education, Rockhampton, Australia, in 1988, and the M.Eng. and Ph.D. degrees from The University of New South Wales, Canberra, ACT, Australia, in 1991 and 1995, respectively, all in electrical engineering.

He was a Lecturer from 1996 to 1999 and a Senior Lecturer from 2000 to 2009 with the School of Electrical Engineering and Information Technology, The University of New South Wales, where he is currently an Associate Professor. His research interests include video and audio coding, medical imaging, data compression, information security, data networks, and error-resilient data transmission.